Nonlocal electron kinetics in a planar inductive helium discharge

Sang-Hun Seo,* Chin-Wook Chung, Jung-In Hong, and Hong-Young Chang
Department of Physics, Korea Advanced Institute of Science and Technology, Taejon 305-701, South Korea
(Received 19 July 1999; revised manuscript received 16 February 2000)

A measurement of the electron energy distribution function (EEDF) using the ac superposition method is done over a helium pressure range of 10–100 mTorr in a planar inductive plasma, and the electron energy diffusion coefficient which describes the electron heating is calculated based on the same discharge conditions using a two-dimensional simulation. It is found that the measured EEDF shows a bi-Maxwellian distribution with a low-energy electron group at low pressures below 20 mTorr even in the inductive discharge using helium of the non-Ramsauer gas. The major factors which can affect the EEDF formation are investigated. In particular, the concept of the total electron bounce frequency, i.e., the electron residence time, is introduced as an indicator of how the electron-electron collision affects the EEDF shape. As a result, it is shown that the observed bi-Maxwellian distribution at low pressures is attributed to the combined effects of the formation of low-energy electrons through the cooling mechanism of energetic electrons enhanced by the capacitive field, the low heating rate of the low-energy electrons, the confinement of low-energy electrons by the ambipolar space potential, and the low electron-electron collision frequency which can be estimated from the total electron bounce frequency presented in this paper.

PACS number(s): 52.40.Db, 52.50.Gj, 52.65.−y, 52.80.−s

I. INTRODUCTION

As feature size dimensions have shrunk in recent plasma etching processes, high-density plasmas operating at low pressures (1–100 mTorr) have been required to obtain good anisotropic patterns and high etching throughput. Among several plasma sources such as electron cyclotron resonance, helicon plasma, and inductively coupled plasma (ICP, including planar-type ICP and cylindrical-type ICP), ICP has been the focus of keen interest as a new and efficient source for semiconductor manufacturing, because low-pressure ICP's have many attractive aspects such as their simple apparatus due to a lack of an external magnetic field, relatively efficient plasma generation (i.e., a relatively high density of $10^{10}-10^{12}\,\mathrm{cm}^{-3}$), good spatial uniformity, low and independently controllable ion energy, and scalability to large-area (for 12-in. wafer) plasma sources. Because low-pressure operation for plasma generation is desirable in modern plasma processing applications, much research on the discharge mechanism itself [1–16] as well as on the plasma processing [17–21] in inductive discharge operating in this regime have been pursued.

Although ICP's have been under development for more than a century since the first report about an electrodeless ring discharge by Hittorf in 1884 [17], studies on the ICP discharge mechanism operating at low pressure have not been extensive until recently. Recently, an ICP heating mechanism in this regime was suggested in Refs. [1] and [2], theoretically and experimentally, respectively. Ohmic heating (collisional heating), randomized by collisions, especially electron-neutral collisions, is dominant at high pressure, where the electron mean free path for the momentum transfer λ is smaller than the skin depth δ of the rf field, and the mean electron momentum transfer frequency ν is much larger than the angular frequency of the rf field ω ($\lambda \ll \delta$ and $\nu \gg \omega$). On the other hand, collisionless heating is widely accepted as the primary heating mechanism in sustaining low-pressure inductive rf discharge ($\lambda \gg \delta$ and $\nu \ll \omega$). Electron heating is a statistical process in which the energy acquired from the field by electrons is converted to randomized electron thermal energy. Thus a phase-breaking (phase-randomization) mechanism that transfers electron momentum is needed [22]. While at high pressures, electron collisions with neutral species are responsible for this conversion process, at low pressures, the phase-breaking is caused by the thermal motion of electrons through the skin layer of rf fields. Turner [1] suggested the existence of the collisionless heating mechanism by calculating the surface impedance of a planar slab using a particle-in-cell Monte Carlo simulation, and the authors of Ref. [2] found it by measuring the external electrical characteristics and the electron energy distribution function (EEDF), respectively. The spatial dispersion of plasma conductivity by this thermal electron motion underlies the anomalous skin effect in the penetration of rf fields and leads to nonmonotonical distribution of rf field and current density [23]. Phenomena such as the nonmonotonic distribution of the rf field and the current density and the local negative power absorption [24] were recently proved through the measurements of the rf field with magnetic probe.

Heating in low-pressure ICP is a combined effect of collisionless power dissipation with the phase-breaking due to the thermal motion of electrons and an anomalous skin effect of an incident rf field [22]. In a weakly ionized low-pressure discharge, electron collisions with neutral species are more frequent than collisions between charged particles. However, since the electron energy relaxation length $\lambda_\varepsilon = \sqrt{\lambda \lambda^*}$ (λ is the electron transport mean free path, and λ^* the mean free path for inelastic collisions) is comparable to or larger than the whole plasma dimension L in this regime, the nonlocal property in the electron kinetics is predominant. The rf elec-

*Electronic address: seosh@cais.kaist.ac.kr

 ©2000 The American Physical Society

tric field induced by the oscillating rf magnetic field rapidly vanishes with increasing distance from the coil due to the diamagnetic property of the plasma, as well as to the geometric effect. The electron heating is therefore spatially inhomogeneous, and occurs mainly near the plasma boundary in the vicinity of the coil. On the other hand, although the heating occurs in the region of a high rf field near the coil, maximum ionization is produced near the maximum of the plasma potential where the rf field is absent [5,25]. As a result, there is a discrepancy in space between the place of the electron heating and the place where the electron energy relaxation occurs. This spatial discrepancy is a major feature of the nonlocal electron kinetics. Since $\lambda_\varepsilon \gg L$ in the nonlocal regime, and since the spatial displacement of electrons occurs faster than their energy relaxation, the electron energy distribution at a specific position in chamber is governed by the discharge properties in the whole volume. Thus the total electron energy $\varepsilon_{\mathrm{tot}}=\varepsilon-eV_p$, where ε and eV_p are kinetic energy and potential energy of an electron, respectively, is a constant motion of the equation, and can be used as an independent variable in the treatment of an electron kinetic equation. In particular, the electron energy distribution can be classified by two energy ranges. In the elastic energy range $\varepsilon<\varepsilon^*$, where ε^* is the first excitation energy, the electrons experience almost elastic collisions with neutrals, i.e., quasielastic collisions. The energy loss in elastic collisions, which is characterized by the average fraction of the energy $\zeta=2m_e/M\ll 1$ lost in a single collision with the atomic gas, the electron-electron Coulomb collisions, and the gas property, and the only mechanisms for electron energy relaxation. Furthermore, since the energy relaxation length of electrons in this energy range exceeds the plasma dimension under nonlocal conditions, and the spatial displacement of electrons occurs rapidly compared to the total energy change due to collisions and heating, the electrons are trapped, and execute a bounce motion in the potential well. In the inelastic energy range of $\varepsilon\geqslant\varepsilon^*$, inelastic collisions (excitation and ionization) with neutrals are probable, and rapid depletions in electron energy distribution occur around each threshold energy. Also, since the plasma potential energy $-e\phi_w$ is larger than the lowest excitation potential of the atoms (or the ionization potential, if direct ionization prevails) due to the faster electron spatial diffusion, there are free electrons with $\varepsilon>-e\phi_w$ as well as trapped electrons with $\varepsilon<-e\phi_w$. It is observed that the electron energy distribution is also depleted at the energy of free electrons that can overcome the plasma potential barrier and escape to the chamber wall [26,12,27].

As previously mentioned, extensive experimental and theoretical studies on the electron heating in low-pressure ICP's have been made. These studies focused in particular on the characteristics of the EEDF for an analysis of electron kinetics under nonlocal conditions. In the theoretical modeling, the so-called nonlocal approach, first suggested by Bernstein and Holstein [28] and Tsendin [29] was used, resulting in a considerable simplification in solving the spatially inhomogeneous Boltzmann equation. In this approach, the total electron energy is used as an independent variable in the Boltzmann equation. The existence of collisionless electron heating was recently revealed by Godyak and Kolobov [13]. Kortshagen measured the spatially resolved EEDF, and presented experimental evidence of nonlocality in electron kinetics [3]. Also, the results of EEDF measurements with various rare gases (Ar, Kr, Xe, Ne, a He:Ar mixture, O_2, and N_2) in the GEC Reference Cell, proposed by Miller *et al.*, were published in Ref. [30]. Although Ar is a fundamental gas in plasma applications, other gases, such as He, Ne, N_2, etc., have frequently been used [31]. However, measurements of the electron energy distribution in experiments using gases other than argon [30] seem to be erroneous, and detailed structures of the EEDFs could not be identified because the energy resolution which can be defined as the energy gap (Δ) between the peak and the zero crossing of the second derivative of the probe characteristic; this is an indicator that the quality of the experiment [32] is not so good ($\Delta\approx 6$ eV).

In this work, an accurate measurement of the EEDF in the rf inductive discharge, using helium as the working gas, is done with the ac superposition method, and notable features appearing at low pressures are presented. Also, the electron energy diffusion coefficient, which can describe electron heating by the inductive field, is calculated using a two-dimensional (2D) simulation. We suggest a parameter of the electron residence time or the electron total bounce frequency which can indicate whether the electrons experience an electron-electron collision or not during their residence time, and we explain this EEDF feature with these parameters. After introducing our experimental methods, including the discharge configuration, the EEDF measurement method, and the rf filtering technique in Sec. II, a calculation of the electron energy diffusion coefficient is presented in Sec. III. The experimental results and a discussion on the EEDF feature is given in Sec. IV. Our conclusions are summarized in Sec. V.

II. EXPERIMENTAL METHODS

A. Experimental apparatus

The experiments employ an inductively coupled plasma (ICP) chamber with an octagonal cross section with a diameter of 36 cm and a length of 30 cm [11]. So as to accurately define the discharge dimension, a plate of adjustable height is supplied and located at 15 cm below the quartz window throughout the experiment. A schematic diagram of the experimental setup is shown in Fig. 1. To simplify the coil geometry, i.e., the field structure, a single-turn coil 20 cm in diameter is placed on a quartz window 30 cm in diameter and 2 cm in thickness. This coil is made of $\frac{1}{4}$-in. copper tube, and coated with silver to prevent surface oxidation. An aluminum kettle covered the coil to protect the measurement apparatus from rf noise. The rf power system consists of a rf signal generator and a power amplifier. The rf signals are supplied by a synthesized rf signal generator (Giga-tronics, 6062A) and amplified by an rf power amplifier (ENI, Model A1000) with a frequency range from 0.3 to 35 MHz and a maximum power of 1000 W. The amplified rf power is applied to an induction coil through the standard type of a matching network. The forward and reflected powers are monitored with a rf power meter (Bird electronics Co.) placed between the rf power amplifier and the matching network.

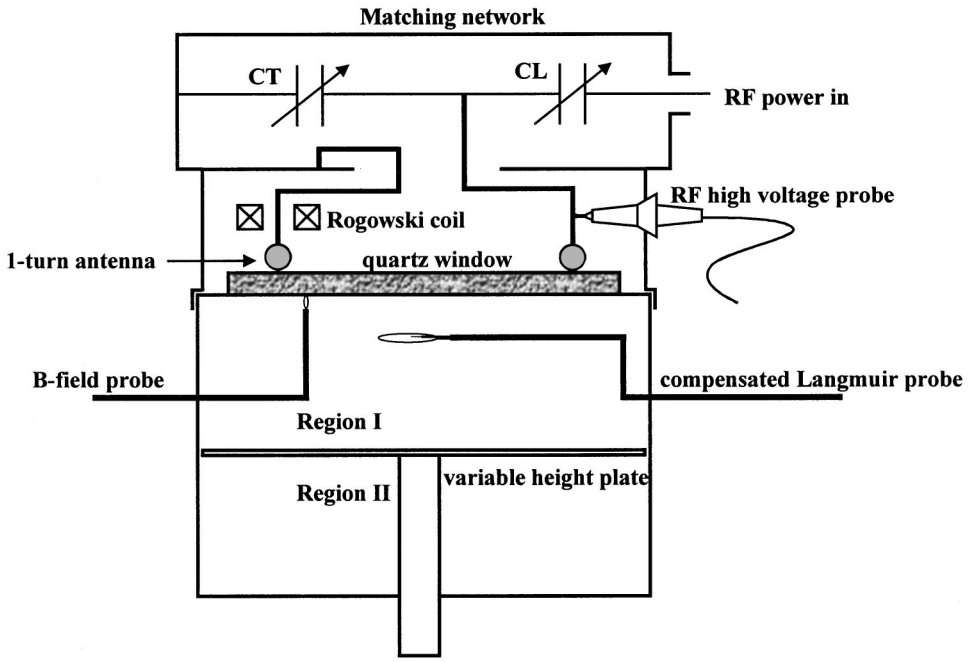

FIG. 1. Schematic diagram of the planar ICP chamber.

B. rf noise filtering

A probe is introduced from the side wall of the chamber. To reduce the rf distortion of the probe characteristics, a probe system consisting of a small measurement probe and a floating-loop reference probe with a self-resonant filtering technique (a tuned probe) is used, as shown in Fig. 2 [12,32]. The measurement probe tip is made of a tungsten wire 4 mm in length and 100 μm in diameter, which is small compared to the electron mean free path for all pressures, and is supported by a capillary sleeve of ceramic tube (2 mm in diameter) in order to prevent electrical contacts between the probe tip and any material sputtered on the probe tip holder. The reference probe, constructed of a tungsten wire 500 μm in diameter and 50 mm in loop diameter, is capacitively connected to the measurement probe with a small film capacitor inside the probe holder. The plasma-to-probe sheath capacitance established by the reference probe is connected in parallel with that by the measurement probe, and thus increases the total sheath capacitance. This decreases the rf input sheath impedance across the probe sheath. As a result, the rf sheath impedance becomes small enough to minimize the plasma rf potential and rf distortions across the probe sheath. A large rf fluctuation of the plasma potential, to the extent of a few mV, which is much larger even in the *E*-mode discharges, can be picked up in the probe circuit. However, while the harmonic components of the rf fluctuation of the plasma potential, especially the second-harmonic component, are significant in symmetrically excited or asymmetric CCP, it can be found, from an investigation of the rf plasma potential spectra, that the magnitude of the second-harmonic component is much smaller (-20 dB) than that of the fundamental component in the present discharge system. Because this seriously distorts the EEDF in spite of small rf noises, rf resonant filters, which can present a large input impedance of the probe circuit to the rf fluctuations, are employed to compensate for the rf fluctuation of the plasma potential, as shown in Fig. 2. Since the rf self-resonant filter cannot be adjusted near the probe tip and is connected close behind the probe holder, a stray capacitance (about 30 pF in our probe system) between the probe tip and the probe holder might reduce the rf impedance of the probe system. Thus, an additional LC series filter is constructed between the probe and the probe circuit in parallel with the self-resonant filter. These resonant filters are tuned to maximize the floating potential. Subsequently, a fine tuning for obtaining a better energy resolution (i.e., small Δ) by further reducing rf noise, proceeds by monitoring the second derivative signal of the probe current.

Besides rf noise suppression, an additional problem, caused by the finite probe circuit resistance, must be considered in the probe diagnostics of high-density rf plasma. Since the probe sheath differential resistance $R_p=(dI_p/dV_p)^{-1} \approx (T_e/e)/I_p$ becomes small as the collected probe current increases, this may lead to a distortion in the low-energy part of the EEPF if the probe circuit resistance R_c is larger than or comparable to R_p, whose minimum value $R_{p\,\mathrm{min}} \approx (T_e/e)/I_{es}$ becomes less than about 30 Ω in our experimental conditions. To solve this problem, a probe current-to-voltage converter as a gyrator with negative input impedance [33] was designed and, thus, the measurement probe was virtually laid on ground potential for all discharge conditions resulting in $R_c \ll R_{p\,\mathrm{min}}$.

C. EEDF measurement

A low-pressure discharge often has an electron energy distribution that departs significantly from the Maxwellian. For example, the electron energy distributions of a low-pressure argon CCP [32] and an argon ICP [12] in the *E* mode are given, which can be approximately by a two-temperature Maxwellian. For a non-Maxwellian and isotropic distribution, the Druyvesteyn analysis for the EEDF measurements is popular and very reliable [17]. The second derivative with respect to the probe potential is proportional to the EEPF $f(\varepsilon)$, and related to the EEDF $g(\varepsilon) = \varepsilon^{1/2} f(\varepsilon)$, by the Druyvesteyn formula [11]:

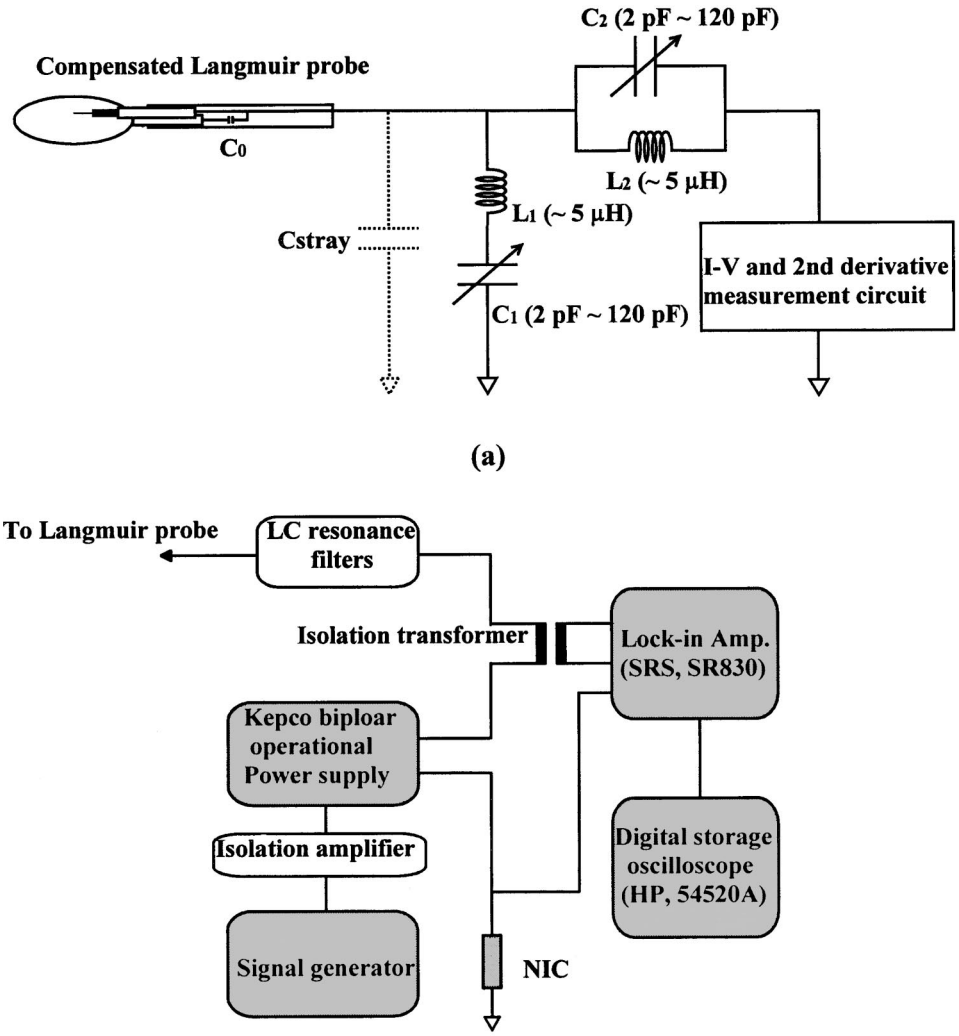

FIG. 2. (a) The cross-sectional view of a compensated Langmuir probe and the circuit diagram of a rf resonant filter. (b) The simplified diagram of the EEDF measurement circuit.

$$g(\varepsilon)=\frac{2m_e}{e^2A_p}\left(\frac{2eV}{m_e}\right)^{1/2}I_p''(V),\quad eV\equiv\varepsilon, \tag{1}$$

where e and m_e are the electron charge and mass, respectively, I_p'' is the second derivative with respect to the probe potential, $V=V_p-V_b$ is the probe potential referenced to the plasma dc space potential, and A_p is the surface area of the probe tip.

The EEDF measurements are done at midplane of the chamber and 5 cm below the dielectric quartz window, and the ac superposition technique [34], which has the advantage of low output noise, is used for the acquisition of the second derivative of the probe characteristic which is proportional to the EEPF from Eq. (1). This technique is the method of superimposing an ac signal v_{ac} on the probe and detecting a harmonic component corresponding to the derivative, and several types of ac signal combinations are available for v_{ac} and the detection frequency component. To simplify the measurement circuit and to reduce the distortion owing to other harmonic components [34] the second-harmonic method was adopted. The measuring circuit is shown in Fig. 2. In this case, a sinusoidal signal ($v_{\mathrm{ac}}=v_0\sin\omega_0 t$) with a small amplitude v_0 and a specific frequency ω_0 is superimposed on the slowly varying probe bias V_b. Using the Taylor series expansion because $v_0\ll V_b$, the amplitude of the second-harmonic component $I_{2\omega_0}$ can be written as

$$I_{2\omega_0}(V_b)=\frac{v_0^2}{4}I_p''(V_b)+\frac{v_0^4}{48}I_p^{(4)}(V_b)+\frac{v_0^6}{1536}I^{(6)}+\cdots. \tag{2}$$

Since v_0 is small and the distortion parameter, defined as the ratio of the signal amplitudes between the second-harmonic Ξ_2 and the fourth-harmonic components Ξ_4, is very small ($\Xi_4/\Xi_2=0.0834v_0$), the contribution of the fourth-harmonic component is negligible. Thus

$$I_{2\omega_0}(V_b)\approx\frac{v_0^2}{4}I_p''(V_b). \tag{3}$$

The probe is biased by a Kepco bipolar operational amplifier activated with a triangular wave from a function generator. A lock-in amplifier (SRS, SR830 DSP Lock-in Amplifier) supplies an ac sinusoidal signal of small amplitude

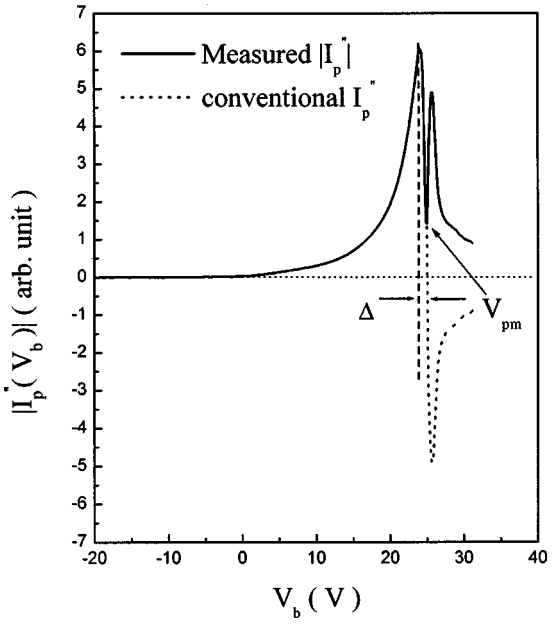

FIG. 3. Second derivative of an *I-V* probe characteristic in the helium ICP ($p=20$ mTorr, $P_{\rm rf}=525$ W).

less than 0.5 zero-to-peak value and a modulation frequency of 10 kHz, and detects the absolute value of $I_{2\omega_0}$. This ac signal is introduced to the probe via an isolation transformer which is calibrated for the frequency of the input signal, and has a small internal resistance of 5 Ω. The signals detected with the lock-in amplifier are ensemble averaged, and recorded with a digital storage oscilloscope (HP, 54520). Each averaged I_p'' is usually based on 64 probe sweeps to improve the signal-to-noise ratio. Although this method has the disadvantage of a slow sweep speed, due to the response of the lock-in amplifier, this can be overcome because the insensitivity to noise in the lock-in detection makes possible a smaller number of averages, so the measurement can be completed within a short time.

Such macroscopic parameters as the electron density n_e and the effective electron temperature $T_{\rm eff}$ can be obtained with the measured EEDF. n_e is calculated by integrating over the EEDF according to

$$n_e=\int_0^{\varepsilon_{\max}} g(\varepsilon)d\varepsilon, \tag{4}$$

where $\varepsilon_{\max}$ is determined by the dynamic range of the EEDF measurement. The effective electron temperature $T_{\rm eff}$ corresponding to a mean electron energy (ε) is also calculated from the second derivative of the probe current as follows:

$$T_{\rm eff}=\frac{2}{3}\langle\varepsilon\rangle\equiv\frac{2e}{3}\frac{\int_0^{\varepsilon_{\max}}\varepsilon g(\varepsilon)d\varepsilon}{\int_0^{\varepsilon_{\max}} g(\varepsilon)d\varepsilon}$$

$$=\frac{2e}{3n_e}\int_0^{\varepsilon_{\max}}\varepsilon g(\varepsilon)d\varepsilon. \tag{5}$$

Also, the plasma potential is found from the minimum point of the absolute value of the second derivative, $|I_p''(V)|$ [12], as shown in Fig. 3.

After the fine tuning of two rf filters, a sample of the $|I_p''(V)|$ measured at a discharge condition of $p=20$ mTorr and $P_{\rm rf}=525$ W is presented in Fig. 3. The difference of this second derivative curve from the previous typical curves is shown in the high-voltage region above the plasma potential, and there is no zero-crossing point. Thus the plasma potential is determined from the minimum point of this curve, as presented in Fig. 3. Also, it is found from this figure that the compensation of rf noise is well achieved and the energy resolution of our EEDF measurement system is very good $(\Delta\lesssim 1$ eV).

III. NUMERICAL APPROACHES

A. Kinetic equations for the EEDF and electron energy diffusion coefficient

The kinetic equation for the electron distribution function (EDF) $\mathcal{F}(\mathbf{r},\mathbf{v},t)$ is

$$\frac{\partial\mathcal{F}}{\partial t}+\nabla_{\mathbf{r}}\cdot(\mathbf{v}\mathcal{F})-\frac{e}{m_e}\nabla_{\mathbf{v}}\cdot[(\mathcal{E}+\mathbf{v}\times\mathcal{B})\mathcal{F}]=S(\mathcal{F}), \tag{6}$$

where $\mathcal{E}$ and $\mathcal{B}$ are the electric and magnetic field, respectively, and $S(\mathcal{F})$ is the collisional integral.

In weakly ionized low-pressure discharges, electron collisions with neutrals dominate over collisions between the charged particles, and the total inelastic collision frequency ν^* is small compared to the electron momentum transfer collision frequency ν. Furthermore, since the spatial scale of the electric heating becomes small in comparison to the electron momentum collision mean free path λ, the electric and magnetic fields can be separated into two parts

$$\mathcal{E}=\mathbf{E}_0+\tilde{\mathbf{E}},\quad \mathcal{B}=\mathbf{B}_0+\tilde{\mathbf{B}}, \tag{7}$$

where $\mathbf{E}_0$ and $\mathbf{B}_0$ are the dc space electric and magnetic fields, which have large spatial scales compared to λ, while $\tilde{\mathbf{E}}$ and $\tilde{\mathbf{B}}$ are the rf electric and magnetic fields, respectively with small scales of $1/k$ compared to λ (i.e., $k\lambda\gg 1$, where k is the wave number of the rf fields).

Assuming that the energy gained during the field period is smaller than the characteristic energy of electrons (i.e., $\Delta\varepsilon \ll \partial\ln\mathcal{F}/\partial\varepsilon$), the conventional two-term approximation is applicable [35],

$$\mathcal{F}(\mathbf{r},\mathbf{v},t)=f_0(v,t)+\tilde{f}_1(\mathbf{r},\mathbf{v},t), \tag{8}$$

where f_0 is the isotropic part of the EEDF which is averaged over a scale in the order of λ, and $\tilde{f}_1$ is the perturbed EEDF $(\tilde{f}_1\ll f_0)$ that describes the deviations of the EEDF on scales smaller than λ. Since the rf field frequency ω is larger than ν $(\omega\gg\nu)$, it is assumed that $f_0(v,t)\approx f_0(v)$ and the energy diffusion coefficient is calculated with neglect of the electrostatic potential in the plasma (rectangular potential well) in this paper as in Ref. [12], with the assumption of the independence of electron density and temperature on the spatial coordinate.

Thus the linearized kinetic equations are written as follows:

$$-\frac{e}{m_e}\nabla_{\mathbf{v}}\cdot[(\tilde{\mathbf{E}}+\mathbf{v}\times\tilde{\mathbf{B}})\tilde{f}_1]=S(f_0), \tag{9}$$

$$\frac{\partial\tilde{f}_1}{\partial t}+\mathbf{v}\cdot\nabla_{\mathbf{r}}\tilde{f}_1-\frac{e}{m_e}\nabla_{\mathbf{v}}\cdot[(\tilde{\mathbf{E}}+\mathbf{v}\times\tilde{\mathbf{B}})\tilde{f}_0]=S(\tilde{f}_1). \tag{10}$$

Averaging the left-hand side of Eq. (9) over space and time, the quasilinear collision integral describing the interaction of the electrons with the rf fields can be obtained as

$$S_{ql}(f_0)=-\frac{e}{m_e}\langle\nabla_{\mathbf{v}}\cdot[(\tilde{\mathbf{E}}+\mathbf{v}\times\tilde{\mathbf{B}})\tilde{f}_1]\rangle_{\mathbf{r},t}, \tag{11}$$

where the $\langle\cdots\rangle_{\mathbf{r},t}$ brackets indicate the spatial and temporal averaging. Furthermore, averaging Eq. (11) over the velocity angle space, the kinetic equation for the isotropic part of the EDF is yielded [35],

$$S^0_{ql}(f_0)\equiv-\frac{e}{m_e}\int\frac{d\Omega_v}{4\pi}\langle\nabla_{\mathbf{v}}\cdot[(\tilde{\mathbf{E}}+\mathbf{v}\times\tilde{\mathbf{B}})\tilde{f}_1]\rangle_{\mathbf{r},t}=S^*(f_0), \tag{12}$$

where $S^0_{ql}(f_0)$ is the quasilinear collision integral averaged over the velocity angles, $d\Omega_v$ is the solid angle in velocity space, and $S^*(f_0)$ is the inelastic collision integral.

If both the equilibrium plasma density and electron temperature are assumed to have no z dependence, the collision operator $S(\tilde{f}_1)$ in Eq. (10) can be approximated by a Krook model, i.e., $S(\tilde{f}_1)=-\nu\tilde{f}_1$. Assuming such time dependence as $\tilde{\mathbf{E}}=\hat{\theta}E_\theta e^{-i\omega t}$ and $\tilde{f}_1=f_1e^{-i\omega t}$, we simplify Eq. (10) to

$$-i\omega f_1+v_z\frac{\partial f_1}{\partial z}-\frac{eE_\theta}{m_e}\frac{\partial f_0}{\partial v_\theta}=-\nu f_1, \tag{13}$$

where the nonlocal behavior of the electrons about the radial inhomogeneity of the inductive electric fields were neglected [10] because

$$\frac{v_r\partial f_1/\partial r}{v_z\partial f_1/\partial z}\sim\frac{v_{th}\partial f_1/\partial r}{v_{th}\partial f_1/\partial z}\sim\frac{\delta}{R}\ll 1, \tag{14}$$

where δ is skin depth, R the radius of the plasma, r the radial coordinate with respect to the chamber center, and z the axial coordinate in the direction of the plasma region from the antenna. With the assumption that the anisotropic part $\tilde{f}_1$ has $e^{-i\omega t}$, the following relation about the time average holds:

$$\langle\nabla_{\mathbf{v}}\cdot[(\tilde{\mathbf{E}}+\mathbf{v}\times\tilde{\mathbf{B}})\tilde{f}_1]\rangle_{\mathbf{r},t}=\tfrac{1}{2}\,\mathrm{Re}[\langle\nabla_{\mathbf{v}}\cdot[(\tilde{\mathbf{E}}^*+\mathbf{v}\times\tilde{\mathbf{B}}^*)\tilde{f}_1]\rangle_{\mathbf{r}}], \tag{15}$$

where * denotes the complex conjugation. Here, f_1 and E_θ can be expanded by the Fourier and the Hankel (Fourier-Bessel) transformation without loss of generality, respectively, as

$$f_1=\sum_{n=0}^{\infty}{}'\ f_n^{(c)}\cos(k_nz)+\sum_{n=1}^{\infty}f_n^{(s)}\sin(k_nz),$$

$$E_\theta=\sum_{m=1}^{\infty}\sum_{n=0}^{\infty}{}'\ E_{mn}J_1\left(\alpha_{1,m}\frac{r}{R}\right)\cos(k_nz), \tag{16}$$

where $k_n\equiv n\pi/L$ is the wave number of the nth Fourier component, J_1 is the first-order Bessel function, $\alpha_{1,m}$ is the mth zero of J_1, and the prime on the summation indicates that the term $n=0$ is multiplied by $\frac{1}{2}$. The Neumann function $N_n[\alpha_{1,m}(r/R)]$ is discarded in Eq. (16) from the condition, where E_θ must be finite at $r=0$.

Substituting Eq. (16) into Eq. (10), $f_n^{(c)}$ and $f_n^{(s)}$ can be obtained as

$$f_n^{(c)}=\frac{ie}{m_e\omega}\frac{\partial f_0}{\partial v_\theta}\sum_{m=1}^{\infty}\frac{E_{mn}J_1(\alpha_{1,m}r/R)}{2}\times\left[\frac{1}{(1-k_nv_z/\omega)+i(\nu/\omega)}+\frac{1}{(1+k_nv_z/\omega)+i(\nu/\omega)}\right], \tag{17}$$

$$f_n^{(s)}=-\frac{e}{m_e\omega}\frac{\partial f_0}{\partial v_\theta}\sum_{m=1}^{\infty}\frac{E_{mn}J_1(\alpha_{1,m}r/R)}{2}\times\left[\frac{1}{(1-k_nv_z/\omega)+i(\nu/\omega)}-\frac{1}{(1+k_nv_z/\omega)+i(\nu/\omega)}\right].$$

Thus, using Eqs. (12) and (15), and applying the Fourier transformation to Eq. (12), we can obtain the averaged quasilinear collision integral as follows:

$$\begin{aligned}S^0_{ql}&=-\frac{e}{2m_e}\int\frac{d\Omega_v}{4\pi}\mathrm{Re}[\langle\nabla_{\mathbf{v}}\cdot[(\tilde{\mathbf{E}}^*+v\times\tilde{\mathbf{B}}^*)\tilde{f}_1]\rangle_{\mathbf{r}}]\\&=-\mathrm{Re}\left[\frac{2}{LR^2}\int_0^L dz\int_0^R r\,dr\,\frac{ie^2}{2m_e^2v^2\omega}\frac{\partial}{\partial v}v^2\right.\\&\quad\times\left\{\sum_{m=1}^{\infty}\sum_{n=0}^{\infty}{}'\ E^*_{mn}J_1\left(\alpha_{1,m}\frac{r}{R}\right)\cos(k_nz)\right.\\&\quad\times\sum_{m'=1}^{\infty}\sum_{n'=0}^{\infty}{}'\ E_{m'n'}J_1(\alpha_{1,m'}r/R)\int\frac{d\Omega_v}{4\pi}(\hat{\mathbf{v}}\cdot\hat{\mathbf{E}})^2\\&\quad\left.\left.\times\left(\frac{1}{[1-(k_{n'}v_z/\omega)]+i(\nu/\omega)}\right)\frac{\partial f_0}{\partial v}\cos(k_{n'}z)\right\}\right],\end{aligned} \tag{18}$$

where $\hat{\mathbf{v}}$ and $\hat{\mathbf{E}}$ are the unit vectors of the electron velocity and the rf electric field, respectively. Here we have used the following relation:

$$\int\frac{d\Omega_v}{4\pi}(\hat{\mathbf{v}}\cdot\hat{\mathbf{E}})^2\left\{\frac{1}{[1-(k_nv_z/\omega)]+i(\nu/\omega)}\right\}=\int\frac{d\Omega_v}{4\pi}(\hat{\mathbf{v}}\cdot\hat{\mathbf{E}})^2\left\{\frac{1}{[1+(k_nv_z/\omega)]+i(\nu/\omega)}\right\}. \tag{19}$$

Applying the orthogonality condition

$$\int_0^R J_1\left(\alpha_{1,m'}\frac{r}{R}\right)J_1\left(\alpha_{1,m}\frac{r}{R}\right)r\,dr=\frac{R^2}{2}J_2^2(\alpha_{1,m})\,\delta_{mm'},$$

$$\int_0^L\cos(k_nz)\cos(k_{n'}z)dz=\frac{L}{2}\,\delta_{nn'}, \tag{20}$$

Eq. (18) can be simplified as follows:

$$S_{ql}^0 = -\int \frac{d\Omega_v}{4\pi} \mathrm{Re}\left[\frac{ie^2(\hat{\mathbf{v}}\cdot\hat{\mathbf{E}})^2}{4m_e^2 v^2 \omega} \frac{\partial}{\partial v} v^2 \times \left(\sum_{m=1}^{\infty} \sum_{n=0}^{\infty}{}' \frac{|E_{mn}|^2 J_2^2(\alpha_{1,m})}{[1-(k_n v_z/\omega)]+i(\nu/\omega)} \frac{\partial f_0}{\partial v} \right) \right]$$

$$= -\frac{e^2}{4m_e^2 v^2 \omega} \frac{\partial}{\partial v} \left(v^2 \int \frac{d\Omega_v}{4\pi} \sum_{m=1}^{\infty} \sum_{n=0}^{\infty}{}' \times \frac{(\nu/\omega)(\hat{\mathbf{v}}\cdot\hat{\mathbf{E}})^2 |E_{mn}|^2 J_2^2(\alpha_{1,m})}{(\nu/\omega)^2+[1-(k_n v_z/\omega)]^2} \right) \frac{\partial f_0}{\partial v}. \quad (21)$$

Here the averaged quasilinear collision integral can be rewritten as [35]

$$S_{ql}^0 = -\frac{1}{v} \frac{\partial}{\partial \varepsilon} (v \mathcal{D}_\varepsilon) \frac{\partial f_0}{\partial \varepsilon}, \quad (22)$$

where $\varepsilon = \frac{1}{2} m_e v^2$, and $\mathcal{D}_\varepsilon$ is the energy diffusion coefficient, which describes the electron heating by inductive electric field. Equating Eqs. (21) and (22), and defining θ_v as the angle between the electric field and the electron velocity in the velocity angle space, $\mathcal{D}_\varepsilon$ takes the following form:

$$\mathcal{D}_\varepsilon = \frac{e^2 \varepsilon}{2m_e \omega} \sum_{m,n}{}' J_2^2(\alpha_{1,m}) |E_{mn}|^2 \Theta\left(\frac{k_n v}{\omega}, \frac{\nu}{\omega} \right), \quad (23)$$

where the function $\Theta(k_n v/\omega, \nu/\omega)$, which represents the phase correlations in the interactions between an electron with thermal velocity v and the electric field E_θ, is defined as

$$\Theta(\alpha_n, \beta) = \frac{1}{4\pi} \int_0^\pi d\theta_v \int_0^{2\pi} d\phi_v \times \frac{\beta \sin\theta_v \cos^2\theta_v}{\beta^2 + (1-\alpha_n \sin\theta_v \cos\phi_v)^2}, \quad (24)$$

with $\alpha_n \equiv k_n v/\omega$ and $\beta \equiv \nu/\omega$.

B. Maxwell equations

The wave equation extended to the infinitely periodic system can be rewritten by [10]

$$\frac{\partial^2 E_\theta}{\partial r^2} + \frac{1}{r}\frac{\partial E_\theta}{\partial r} - \frac{E_\theta}{r^2} + \frac{\partial^2 E_\theta}{\partial z^2} + \kappa^2 E_\theta = -\frac{4\pi\kappa}{c} i J_p - 2i\kappa \sum_{n=-\infty}^{\infty} B_r(r, z_n+0)\, \delta(z-z_n), \quad (25)$$

where $z_n \equiv nL$, $\delta(z)$ is the Dirac δ function, and

$$B_r(r, z_n+0) \equiv \lim_{\varepsilon\to 0} B_r(r, z_n+\varepsilon), \quad (26)$$

$$B_r(r, z_n-0) \equiv \lim_{\varepsilon\to 0} B_r(r, z_n-\varepsilon) = -B_r(r, z_n+0) \quad \text{for } \varepsilon \geqslant 0.$$

The boundary conditions are

$$E_\theta(R,z) = 0, \quad E_\theta(r,L) = 0, \quad B_r(r,0) = B_0 = \frac{i}{\kappa} \left. \frac{\partial E_\theta(r,z)}{\partial z} \right|_{z=0}, \quad (27)$$

where $\kappa = \omega/c$ is the vacuum wave number. Using the Fourier-Bessel transformation for the rf electric field and the rf plasma current and boundary condition (27), the Fourier-Bessel component of the inductive field E_{mn} is given by [15]

$$E_{mn} = \frac{2i\kappa\lambda_{\mathrm{eff}}^2}{L} \left[1-(-1)^n \frac{\xi_{2m}}{\xi_{1m}} \right] \frac{b_{0m}}{D_{mn}}, \quad (28)$$

where $\lambda_{\mathrm{eff}} = v/\sqrt{\omega^2+\nu^2}$ is an effective mean free path, $\xi_{1m} = 1/(2D_{m0}) + \Sigma_{n=1}^{\infty} 1/D_{mn}$, $\xi_{2m} = 1/(2D_{m0}) + \Sigma_{n=1}^{\infty} (-1)^n/D_{mn}$, and

$$D_{mn} = \begin{cases} h_m^2 + \dfrac{\Lambda}{s} & \text{for } n=0 \\ h_m^2 + q_n^2 - \dfrac{\Lambda}{q_n} Z_p\left(\dfrac{s}{q_n} \right) & \text{(otherwise)}. \end{cases} \quad (29)$$

Here $h_m = \beta_m \lambda_{\mathrm{eff}}$, $\beta_m = \sqrt{(\alpha_{1,m}/R)^2 - \kappa^2}$, $q_n = k_n \lambda_{\mathrm{eff}}$, $s = (\omega + i\nu)/\sqrt{\omega^2+\nu^2}$ is the collisionality of the system, Z_p is the plasma dispersion function [36], and Λ is a measure of the system nonlocality [6] and is written by

$$\Lambda = \left(\frac{v\omega_{\mathrm{pe}}}{c\omega} \right)^2 [1+(\nu/\omega)^2]^{-3/2} = (\lambda_{\mathrm{eff}}/\delta_p)^2, \quad \delta_p = \frac{c}{\omega_{\mathrm{pe}}} \left(1 + \frac{\nu^2}{\omega^2} \right) \frac{1}{\cos(\theta/2)}, \quad (30)$$

where $\theta = \tan^{-1}(\nu/\omega)$ and $\omega_{\mathrm{pe}} = (e^2 n_e/\varepsilon_0 m_e)^{1/2}$ is the electron plasma frequency.

b_{0m} in Eq. (28), which is the Bessel component of the radial induced magnetic field at the plasma surface [10], has the form

$$b_{0m} = \frac{2\pi L}{c} j_{c,m}^{(sh,L_s)} [\sinh(\beta_m L_s) + (2\beta_m/L)\cosh(\beta_m L_s) S_m]^{-1}, \quad (31)$$

where L_s is the distance from the plasma to the top metal plate:

$$j_{c,m}^{(sh,L_s)} = \frac{4}{L_s R^2 J_2^2(\alpha_{1,m})} \int_{-L_s}^0 \int_0^R J_c(r,z) J_1(\alpha_{1,m} r/R) \times \sinh[\beta_m(z+L_s)] r\, dr\, dz, \quad (32)$$

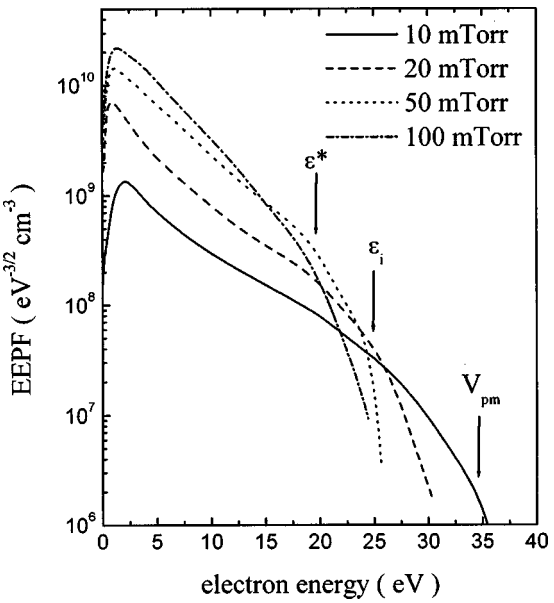

FIG. 4. The EEPF evolution with changing helium pressure at $P_{\mathrm{rf}}=525\,\mathrm{W}$.

$$S_m=\frac{l^2(\xi_{1m}^2-\xi_{2m}^2)}{\xi_{1m}}.$$

Here $J_c(r,z)$ is the antenna coil current density. To determine the antenna current magnitude from the input rf power, we used the relation $|I|=\sqrt{2P_{\mathrm{rf}}/(R_{\mathrm{pl}}+R_c)}$, where P_{rf} is the input rf power, $R_{\mathrm{pl}}=\mathrm{Re}[Z_{\mathrm{pl}}]$, and R_c are the resistance of the plasma and coil, respectively. The plasma impedance Z_{pl} can be determined from the Poynting's theorem, and has the form [10]

$$Z_{\mathrm{pl}}=-\frac{i\omega R^2}{2L}\sum_{m=1}^{\infty}J_2^2(\alpha_{1m})\left|\frac{b_{0m}}{I}\right|^2 S_m. \tag{33}$$

Using Eqs. (28), (31), and (33), the magnitude of E_{mn} in Eq. (23) can be determined from the antenna, plasma, and reactor parameters.

IV. RESULTS AND DISCUSSION

A. EEDF measurement results

The EEDF measurement was carried out at a rf frequency of 13 MHz and a rf power of 525 W over a helium pressure range of 10–100 mTorr and the results are given in Fig. 4 in terms of the EEPF which is proportional to the second derivative of the probe current-voltage (I-V) curve. In general, since the threshold energy of the helium gas for ionization ($\varepsilon_{\mathrm{iz}}$) is much higher than that of the benchmark argon gas ($\varepsilon_{\mathrm{iz}}=15.8$ and 24.6 eV for argon and helium, respectively), the discharge breakdown in the helium discharge is difficult compared to the case of the argon discharge, and much more rf power is required as the gas pressure decreases. In our discharge system, the minimum pressure where discharge breakdown is possible with a rf power of 525 W is 10 mTorr.

As can be seen from Fig. 4, it is remarkable that the low-energy electron groups can develop at low pressures below 20 mTorr even in a non-Ramsauer gas like helium. It has been well known that the bi-Maxwellian EEPF, which can be represented as a sum of two Maxwellian distributions with two electron temperatures T_1 and T_2, is typical in low-pressure argon CCP's [32] and it has been found experimentally [32] and theoretically [32,37,38] that the existence of two electron groups in the low-pressure argon discharge results from stochastic electron heating in the oscillating sheath enhanced by the Ramsauer effect and by low electron-electron collision frequency due to abnormally low electron energy. In the case of low-pressure helium CCP's, while the authors of Ref. [32] could not find the low-energy electron groups in their experimental situation and only argued that it is possible that it may develop in a non-Ramsauer gas like helium, other workers [39] could measure it with a number of low-energy electrons relatively smaller than that found in argon.

On the other hand, this bi-Maxwellian EEDF was found in the inductive argon discharge with [8] and without electrostatic screen [12]. In Ref. [12], when the mode transition from an E mode to an H mode occurs, the evolution of the EEPF from a bi-Maxwellian distribution at low power to a Maxwellian distribution at sufficiently high power was presented. With an electrostatic screen [8], a bi-Maxwellian distribution with a relatively small number of low-energy electrons due to the reduction of the capacitive power coupling was found. In the case of inductive helium discharge, theoretical [16] and experimental [30] approaches were made. However, the low-energy electron group was not found in these works due to the exclusion of the capacitive power coupling in modeling [16] and the low energy resolution in the He/Ar mixture plasma [30]. On the other hand, in our work, the low-energy electron group, i.e., the bi-Maxwellian distribution, can be resolved through the EEDF measurement system with high-energy resolution ($\Delta<2.5\,\mathrm{eV}$), even in low-pressure and inductive helium discharge with capacitive power coupling.

For the experimental condition where the electron energy relaxation length λ_ε is larger than the spatial plasma scale L, the EEDF can be divided into two energy ranges: the elastic range ($\varepsilon<\varepsilon^*$, where $\varepsilon^*=19.8\,\mathrm{eV}$ is the first excitation energy of helium gas) and the inelastic energy range ($\varepsilon>\varepsilon^*$). From Fig. 4, it can be seen that as the gas pressure increases, the measured EEPF within the elastic energy range gradually evolves from a bi-Maxwellian distribution into a Maxwellian distribution, and it has an almost Maxwellian distribution with $T_{\mathrm{eff}}\approx T_{\mathrm{ed}}$, where the distribution temperature T_{ed} is defined as $T_{\mathrm{ed}}=[d(\ln f(\varepsilon))/d\varepsilon]^{-1}$ at pressures above 50 mTorr. On the other hand, in $\varepsilon>\varepsilon^*$ the EEDF experiences depletion due to the inelastic collisions between high-energy electrons and neutral gases as in the case of argon plasma [12]. Since the electron energy relaxation length typically exceeds the length of a bounded plasma at low pressures, the nonlocal property in the electron kinetics predominates, thus the electron energy distribution is affected by the discharge properties in the whole plasma area. One of these features [26] can be seen in the EEDF tail depletion of Fig. 4. At the minimal maintainable gas pressure $p_{\mathrm{min}}=10\,\mathrm{mTorr}$, the first change of EEPF slope is clearly found at $\varepsilon\approx\varepsilon^*$, and the second change is shown at $\varepsilon\approx\varepsilon_i$, as in the case of argon plasma [12]. In particular, the additional steep decrease of the EEPF tail at $\varepsilon\geqslant eV_{pm}$, caused by

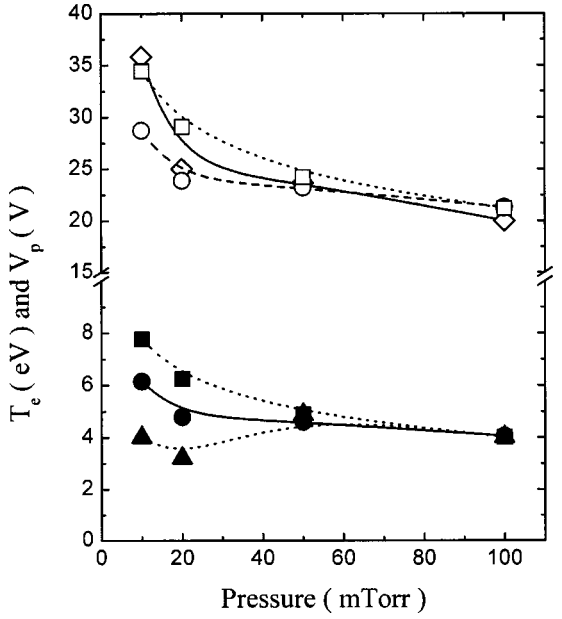

FIG. 5. The trends of the electron temperatures (T_{eff}, T_1, and T_2) and the plasma potentials (V_{pm}, $V_{p\,\text{eff}}$, and V_2) against helium pressure. Solid circle symbols are T_{eff}; solid rectangle, T_2; solid triangle, T_1; open diamond, V_{pm}; open rectangle, V_2; open circle, V_{eff}.

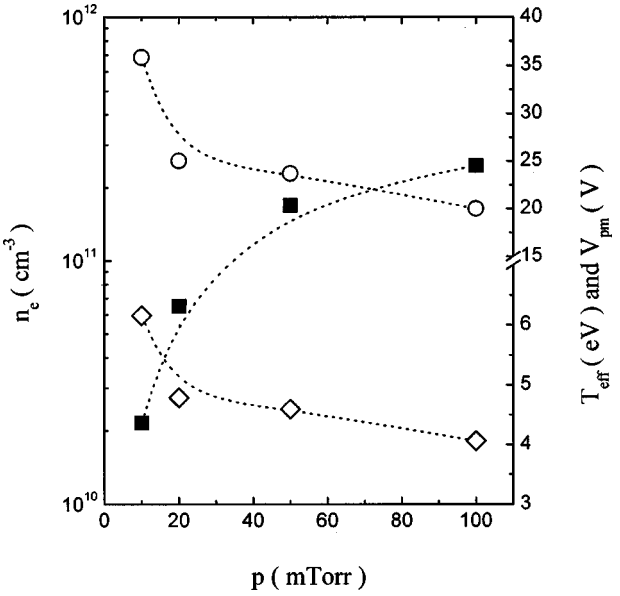

FIG. 6. The trends of n_e, T_{eff}, and V_{pm} against helium pressure. Solid rectangular symbols are n_e; open diamond, T_{eff}; open circle, V_{pm}.

the escape of the energetic electrons to the wall, can also be observed at $p=p_{\min}$.

On the other hand, as the gas pressure increases, the distribution temperature of the EEPF gradually decreases, and the EEPF depletion becomes more and more steep. Also, at the highest pressure of this experiment (100 mTorr), only EEPF depletion near $\varepsilon\approx\varepsilon^*$ can be observed. This is due to the increase in collision frequency between the electrons and helium atoms associated with the increase in the number of helium atom and the decrease in plasma potential due to the decrease in electron temperature. Even at 100 mTorr, the plasma potential becomes similar to the excitation energy level (see Fig. 5).

These bi-Maxwellian EEDF's can be represented by temperatures T_1 and T_2 as [12,14]

$$f(\varepsilon)=A[(1-\beta)e^{-\varepsilon/T_1}+\beta e^{-\varepsilon/T_2}], \tag{34}$$

where $\beta\equiv n_2/n_1$ is the ratio of densities of the two electron groups, and A is obtained from the EEDF normalization. T_1 and T_2, obtained as the distribution temperatures in Fig. 4, are about 4.0 and 7.7 eV at 10 mTorr and 3.2 and 6.2 eV at 20 mTorr. In a plasma with a Maxwellian EEDF, where the collisionless sheath is applicable, a simple relation between the plasma potential and the electron temperature can be obtained using the balance of the electrons and ion fluxes entering the sheath [17,12],

$$\Delta V_w=\frac{kT_e}{2e}\ln\left(\frac{M}{2\pi m_e}\right)\approx 3.5\times\frac{kT_e}{e}, \tag{35}$$

where ΔV_w is the plasma potential with respect to the floating wall, and M the helium ion mass. Substituting T_{eff} and T_2 for T_e in Eq. (35), and using the measured floating potential, the effective plasma potential V_{eff} and the plasma potential V_2 are obtained as presented in Fig. 5. As presented in Ref. [12], when the EEDF becomes a bi-Maxwellian EEDF, the discrepancy between the measured plasma potential V_{pm} and the calculated plasma potential V_{eff} is observed due to the existence of a high-energy electron tail and the generation of the low-energy electron group in the bi-Maxwellian EEDF is enhanced by the capacitive power coupling in ICP. As can be shown in Fig. 5, at low pressures, where the EEDF becomes a bi-Maxwellian EEDF, the plasma potential is primarily governed by the temperature of the high-energy electron tail.

The electron density, the effective electron temperature, and the plasma potential derived from the measured EEPF are shown in Fig. 6. Although the electron density rapidly increases with increasing gas pressure, the effective electron temperature and the plasma potential gradually decrease. Since the discharge chamber is not equipped with an electrostatic screen, the capacitive field as well as the inductive field can participate in the electron heating, especially at low pressures, and this contribution will be very significant at low pressures due to the low electron density. Because the electron density rapidly increases as the gas pressure increases, the capacitive field is more effectively shielded by the plasma and localized near the antenna region, and its contribution to the electron heating becomes gradually weaker. A major reason that no low-energy electrons appear in the theoretical result of Ref. [16] may result from the exclusion of the generation of low-energy electrons by the capacitive power coupling. Also, it can be found that the plasma potential approaches the first excitation energy due to the decrease in the electron temperature as the gas pressure increases [26].

B. Numerical results for the energy diffusion coefficient

From Eq. (22), the electron heating and the shape of the EEDF are determined by $\mathcal{D}_\varepsilon$. Since the energy flux Γ_ε can be written as

$$\Gamma_\varepsilon = -n_e \mathcal{D}_\varepsilon \frac{d\overline{f}}{d\varepsilon}, \quad \overline{f} = \frac{f}{n_e} \tag{36}$$

and the electron heating power density is

$$p_{e\,\mathrm{heat}} = \frac{2\sqrt{2}\pi}{m_e^{3/2}} \int_0^\infty f(\varepsilon) \frac{\partial}{\partial \varepsilon} [\sqrt{\varepsilon} \mathcal{D}_\varepsilon] d\varepsilon, \tag{37}$$

$\mathcal{D}_\varepsilon$ contains all the information about the electron heating process, and the EEDF formation is determined by $n_e \mathcal{D}_\varepsilon$ [5]. In a limiting case where the nonlocality in electron kinetics does not prevail, Eq. (23) approaches the well-known equation for the energy diffusion coefficient. Since electron thermal motion is not important in a cold plasma, $\alpha_n (\equiv k_n v/\omega) \ll 1$, and all modes of the rf electric field equally contribute to electron heating. Under this condition, Eq. (24) is reduced to

$$\Theta \approx \frac{\beta}{3(\beta^2+1)}, \tag{38}$$

and Eq. (23) has an approximation form of

$$\mathcal{D}_\varepsilon \approx \frac{e^2 \langle |E_\theta|^2 \rangle v^2 \nu}{6(\omega^2+\nu^2)}, \tag{39}$$

where

$$\langle |E_\theta|^2 \rangle = \frac{2}{LR^2} \int_0^L dz \int_0^R r\, dr |E_\theta|^2 = \frac{1}{2} \sum_{m,n}{}' J_2^2(\alpha_{1,m}) |E_{mn}|^2 \tag{40}$$

is the mean square of E_θ averaged over the discharge volume. The energy diffusion coefficient $\mathcal{D}_\varepsilon$ in Eq. (39) corresponds to a spatially averaged Joule heating produced by an inhomogeneous rf electric field. It should be noted that for collisional (Ohmic) heating, $\mathcal{D}_\varepsilon$ is a function of the local rf electric field.

In the limit of low collision frequencies ($\nu \ll \omega$) $\Theta(\alpha_n, \beta)$ vanishes when $\alpha_n (= k_n v/\omega) < 1$ and thus, only higher nth Fourier components of rf electric field contributes to the low-energy electron heating. However, since the nth component of the rf electric field becomes significantly weaker at higher n, the heating of low-energy electrons with $v < \omega L/\pi$ becomes inefficient. In the other limit of $\nu \gg \omega$, $\Theta(\alpha_n, \beta) \approx 1/\beta$ from Eq. (24), and $\mathcal{D}_\varepsilon$ has the functional dependence of $1/\nu$. Thus the energy transfer is strongly dependent on the variation of the momentum transfer cross section with the energy in this limit. The most pronounced variation of the cross section is found in the case of argon due to the Ramsauer effect, which was already reported in Ref. [13].

The numerical calculation of the terms in Eq. (23) proceeds until $\mathcal{D}_\varepsilon$ converges over m and n, and the calculated result is presented in terms of $n_e \mathcal{D}_\varepsilon$ in Fig. 7 [see Eq. (36)]. It is seen in Fig. 7 that $n_e \mathcal{D}_\varepsilon$ increases monotonically as a function of ε at all pressures, and its absolute value increases with pressure. This is due to the energy dependence of the momentum transfer cross section, which does not vary much and is almost constant in the low-energy region below 5 eV [17].

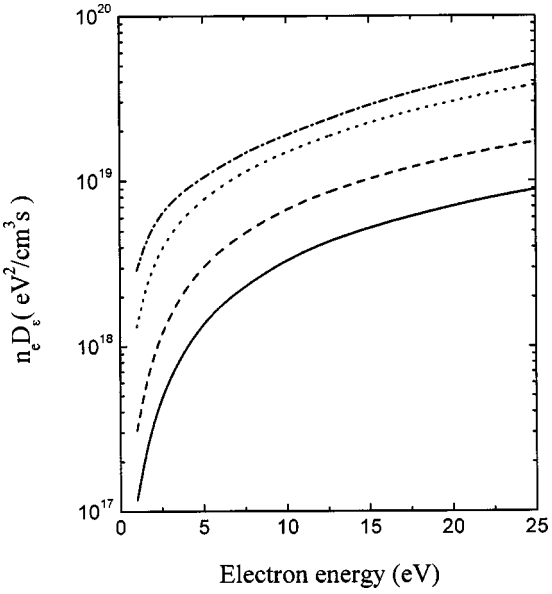

FIG. 7. Space-averaged electron energy coefficients at $p = 10$ (solid line), 20 (dashed line), 50 (dotted line), and 100 mTorr (dash-dotted line).

C. Discussions

As previously mentioned, it is notable that the bi-Maxwellian EEDF can be observed at low pressures in a non-Ramsauer gas like helium. In capacitive argon discharges, the decisive role of the Ramsauer effect on the EEPF formation was discussed in detail in Ref. [32]. On the other hand, in the case of inductive argon discharges, it was reported that the low-energy electron group can develop at low-pressure argon discharges with [8] and without an electrostatic screen [12]. In Ref. [8], although an electrostatic screen, was used, which practically eliminated the capacitive power coupling between the induction coil and the plasma, a low-energy electron group with a distribution temperature less than the effective electron temperature of the EEPF, similar to that found in capacitive rf discharge was observed. Inferring from Refs. [8], [12], [12] the formation of the low-energy electron group is determined by such physical phenomena as the capacitive power coupling between the plasma and the rf induction coil, the energy dependence of the electron heating (which can be found from the energy dependence of the electron energy diffusion coefficient), and various collision processes such as quasielastic collisions (including those with a small energy loss compared to the electron energy [5]) and electron-electron collisions.

In analogy with the cooling mechanism of energetic electrons in low-pressure CCP's, the presence of a low-energy electron group is primarily caused by the capacitive power coupling between the oscillating sheath and the plasma, and by the nonlocal electron kinetics in the discharge condition where $\lambda_\varepsilon \gg L$ [12]. It was already reported that the low-energy electron group observed in a rf argon inductive discharge, with a partially electrostatic screen [3,4] or without an electrostatic screen [12], did not appear when capacitive power coupling from a rf induction coil with a complete electrostatic screen [15] was effectively eliminated. Therefore, its appearance seems to be the result of the capacitive power coupling.

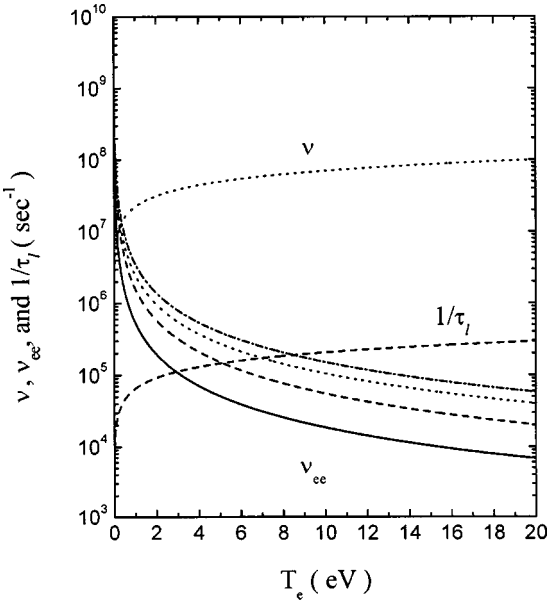

FIG. 8. The total electron bounce frequency (dashed line), the electron-electron collision frequencies, and the electron-neutral collision frequency (dotted line, at 10 mTorr) against the electron temperature for each experimental condition of $p=10$ (solid line), 20 (dashed line), 50 (dotted line), and 100 mTorr (dash-dotted line).

As previously mentioned, the energy diffusion coefficient $n_e\mathcal{D}_\varepsilon$ increases monotonically as a function of ε irrespective of gas pressure. With this energy dependence of the energy diffusion coefficient, the EDF typically has a concave shape at low energies, i.e., a low-energy electron group and a convex shape at high energies that can be characterized by three distribution temperatures with no Coulomb interaction among electrons [7]. Thus, without the Coulomb interaction between electrons, the formation of the low-energy electron group is caused by an inefficient heating of the low-energy electrons, produced by the ionization process and enhanced by the capacitive power coupling, which can be found from the energy dependence of the energy diffusion coefficient and the confinement effect by the space potential. The convex shape in the high-energy range of $\varepsilon>\varepsilon^*$ is due to the energy loss in the inelastic collisions and to wall loss. On the other hand, if the electron-electron Coulomb collision is frequent enough, the electron energy thermalization proceeds rapidly, and the EDF within the elastic energy range appears as a Maxwellian distribution.

In the elastic energy range below 19.8 eV, the quasielastic collisions include those with a small energy loss compared to electron energy [5]. They are characterized by the parameter ζ, which is the average fraction of the energy lost in a single collision, and the electron-neutral collision frequency is written by

$$\nu = N k_{\mathrm{en}}(T_e), \tag{41}$$

where $N[=8.3212\times10^{11}p(\mathrm{mTorr})/T_N(\mathrm{eV})]$ cm^{-3} is the number of neutral species, and $k_{\mathrm{en}}(=20\times10^{-16}\sqrt{8T_e/\pi m_e}$ [40]) the proportional coefficient. Since $\zeta(=2m_e/M)\ll1$ in spite of $\nu\gg\nu_{ee}$ (see Fig. 8), it is permissible to neglect their collision process in the EEDF formation [5]. Not only is the electron heating process determined by the energy dependence of the electron energy diffusion coeffiecient, but the collision process among electrons affects the EEDF formation because sufficiently high electron-electron collisions tend to make the EDF a Maxwellian distribution. The electron-electron collision frequency depends on such plasma parameters as electron density and electron temperature, and can be written as

$$\nu_{\mathrm{ee}} = 2.91\times10^{-6} n_e \ln\Lambda (T_e)^{-3/2}, \tag{42}$$

where ν_{ee} is the electron-electron collision frequency, n_e the electron density per cubic centimeter, and the Coulomb logarithm $\ln\Lambda$ is given by

$$\ln\Lambda = \begin{cases} 23-\ln(n_e^{1/2}T_e^{-3/2}), & T_e\leqslant10\ \mathrm{eV} \\ 24-\ln(n_e^{1/2}T_e^{-1}), & T_e>10\ \mathrm{eV}. \end{cases}$$

On the other hand, since $\lambda^*\gg L$ under the discharge conditions where the nonlocal property in electron kinetics predominates, the bounce motion of electrons becomes important in electron heating. If a typical loss velocity of plasma at the plasma-sheath boundary is the ion Bohm velocity $v_s=\sqrt{T_e/M}$, the electrons bounce v_{th}/v_s times between the sheath boundaries before they escape from the bulk plasma [9]. Thus the total mean free path of electrons for the electron loss λ_l becomes $(2Lv_{\mathrm{th}})/v_s$, and the residence time of electrons defined by $\tau_l=\lambda_l/v_{\mathrm{th}}$ is $2L/v_s$. As a result, if $\tau_l\nu_{\mathrm{ee}}\ll1$, electrons rarely experience electron-electron collision during the time τ_l and, thus, the electron energy thermalization process does not occur very well. But, in the opposite case ($\tau_l\nu_{\mathrm{ee}}\gg1$) electrons collide at least one time with each other during τ_l, and it can be said that the EEDF thermalization occurs, so that the EEDF may evolve into a Maxwellian distribution.

Figure 8 shows the dependences of the electron-electron collision frequency and the total electron bounce frequency ($\equiv1/\tau_l$) on the electron temperature at each electron density measured in this experiment. As known from Eq. (42), since $\ln\Lambda$ is insensitive to electron temperature and is almost constant, the electron-electron collision frequency rapidly decreases with a power factor of $\frac{3}{2}$ as the electron temperature increases. On the other hand, since $1/\tau_l\propto\sqrt{T_e}$, the total electron bounce frequency steadily increases with increasing electron temperature. It can be seen from Fig. 8 that the critical temperatures defined by the electron temperature with which $\tau_l\nu_{\mathrm{ee}}\approx1$ is satisfied increase with increasing electron density. Considering the data of Fig. 5, one sees that the electrons thermalization does not proceed well below pressures of 20 mTorr, because $\tau_l\nu_{\mathrm{ee}}\leqslant1$. Consequently, the low-energy electron group which is produced by inelastic collision processes and enhanced by the capacitive power coupling is not thermalized, and remains in bulk plasma for a long residence time and is confined by the space potential. Thus, under these plasma conditions, the EEDF will have nothing but a bi-Maxwellian distribution with the low-energy electron group.

V. CONCLUSIONS

In conclusion, the exact measurement of the EEDF was made with a rf-compensated Langmuir with two LC resonant

filters and the ac superposition method in a planar inductive helium discharge. With a high signal-to-noise ratio and a high energy resolution, it was possible to measure the EEDF even at the low pressure of 10 mTorr. Unlike the theoretical result of Ref. [16], bi-Maxwellian EEDFs with low-energy electron groups can be observed at low pressures below 20 mTorr in planar inductive discharge without an electrostatic screen. As a result of Ref. [37] where the EEDF was obtained through a particle-in-cell Monte Carlo simulation, even though the Ramsauer effect is artificially removed, the EEDF which appeared obviously as a bi-Maxwellian distribution with the Ramsauer effect remains a bi-Maxwellian distribution in which the equivalent temperature of the high-energy electron group does not change, but the equivalent temperature of the low-energy electron group increases slightly due to the enhancement of the bulk heating by the removal of the Ramsauer effect. In Ref. [32], it was argued that although this bi-Maxwellian distribution is not observed in their experiments in low-pressure helium CCP, it is possible that a low-energy electron group develops in the non-Ramsauer gas with a much greater ω/pd than in their experiments. Therefore, it can be inferred from these reports [37,32] that the low-energy electrons can be generated with stochastic heating in the sheath and negligible bulk heating in the nonlocal regime of electron kinetics, and this situation is similar to the situation of our experiment in ICP except for the effect of electron-electron collisions due to the different electron densities.

The factors which can affect the EEDF shape within the elastic energy range, under discharge conditions where the nonlocal properties in electron kinetics prevail, are heating by the rf field, a specific electron-neutral collision cross section like the Ramsauer minimum, a confinement effect by the ambipolar space potential, and electron thermalization by electron-electron collision. First, because our discharge system does not have any electrostatic screen, the rf fields which can participate in electron heating include the capacitive field and the inductive field. From Refs. [12,15], it can be deduced that electron heating by the capacitive power coupling and the cooling mechanism of energetic electrons are the primary factors in the formation of the low-energy electron group in low-pressure helium ICP. On the other hand, electron heating by the inductive field can be described through a calculation of the electron energy diffusion coefficient. In this work, the energy diffusion coefficient was obtained using a 2D simulation. It was found that the energy diffusion coefficient increases monotonically as a function of ε irrespective of gas pressure, and no enhanced heating in the low-energy part was found, in contrast to the case of the argon discharge [13]. In the modeling result of Ref. [16], the EEDF in the helium discharge is a Maxwellian distribution even in the low electron density of $7\times10^{8}/\mathrm{cm}^{3}$, without any low-energy electron group. This may be attributable to the exclusion of capacitive power coupling, so that a low-energy electron group cannot develop.

The other factor which must be considered in forming the EEDF is electron-electron collision. Since the electron-electron collision frequency is dependent on the electron density and electron temperature as $n_e T_e^{-3/2}$ from Eq. (42), the EEDF becomes a Maxwellian distribution with a single temperature when the electron density is sufficiently high or the electron temperature is very low. In this paper, the electron residence time $\tau_l=\lambda_l/v_{\mathrm{th}}$ is suggested as a parameter to determine whether the electron energy thermalization through electron-electron collision can occur or not. In the present experiment, since $\tau_l\nu_{\mathrm{ee}}\ll1$ at pressures below 20 mTorr (see Fig. 8), the electrons are not well thermalized during their residence time. Therefore, it can be concluded that the development of the low-energy electron group at low pressures below 20 mTorr is due to the combined effects of the formation of a low-energy electron group through the cooling mechanism of energetic electrons heated by the capacitive field, a decrease in the energy diffusion coefficient with electron energy, a confinement of low-energy electrons by the space potential, and a low electron-electron collision frequency which is estimated from $\tau_l\nu_{\mathrm{ee}}\ll1$.

ACKNOWLEDGMENTS

We are grateful to Dr. S. S. Kim and Dr. N. S. Yoon for help with their offer of the 2D antenna modeling code in the energy diffusion coefficient calculations.

[1] M. M. Turner, Phys. Rev. Lett. **71**, 1844 (1993).
[2] V. A. Godyak, R. B. Piejak, and B. M. Alexandrovich, Plasma Sources Sci. Technol. **3**, 169 (1994).
[3] U. Kortshagen, I. Pukropski, and M. Zethoff, J. Appl. Phys. **76**, 2048 (1994).
[4] L. J. Mahoney, A. E. Wendt, E. Barriors, C. J. Richards, and J. L. Shohet, J. Appl. Phys. **76**, 2041 (1994).
[5] V. I. Kolobov and W. N. G. Hitchon, Phys. Rev. E **52**, 972 (1995).
[6] V. I. Kolobov and D. J. Economou, Plasma Sources Sci. Technol. **6**, R1 (1997).
[7] V. I. Kolobov, D. P. Lymberopoulos, and D. J. Economou, Phys. Rev. E **55**, 3408 (1997).
[8] V. A. Godyak and V. I. Kolobov, Phys. Rev. Lett. **81**, 369 (1998).
[9] N. S. Yoon, S. S. Kim, C. S. Chang, and D. I. Choi, Phys. Rev. E **54**, 757 (1996).
[10] N. S. Yoon, S. M. Hwang, and D. I. Choi, Phys. Rev. E **55**, 7536 (1997).
[11] S. Seo, J. Hong, K. Bai, and H. Chang, Phys. Plasmas **6**, 614 (1999).
[12] S. Seo, J. Hong, and H. Chang, Appl. Phys. Lett. **74**, 2776 (1999).
[13] S. Seo, S. S. Kim, J. Hong, C. S. Chang, and H. Chang, Appl. Phys. Lett. **76**, 149 (2000).
[14] V. A. Godyak, V. P. Meytlis, and H. R. Strauss, IEEE Trans. Plasma Sci. **23**, 728 (1995).
[15] V. A. Godyak, R. B. Piejak, and B. M. Alexandrovich, Plasma Sources Sci. Technol. **4**, 332 (1995).
[16] V. I. Kolobov, G. J. Parker, and W. N. G. Hitchon, Phys. Rev. E **53**, 1110 (1996).
[17] M. A. Lieberman and A. J. Lichtenberg, *Principles of Plasma Discharges and Materials Processing* (Wiley, New York, 1994), p. 387

[18] J. Hopwood, Plasma Sources Sci. Technol. **1**, 109 (1992).
[19] J. Hopwood, C. R. Guarnieri, S. J. Whitehair, and J. J. Cuomo, J. Vac. Sci. Technol. A **11**, 152 (1993).
[20] M. S. Barnes, J. C. Forster, and J. H. Keller, Appl. Phys. Lett. **62**, 2622 (1993).
[21] J. A. O'Neil, M. S. Barnes, and J. H. Keller, J. Appl. Phys. **73**, 1621 (1993).
[22] M. A. Lieberman and V. A. Godyak, IEEE Trans. Plasma Sci. **26**, 955 (1998).
[23] V. A. Godyak and R. B. Piejak, J. Appl. Phys. **82**, 1 (1997).
[24] V. A. Godyak and V. I. Kolobov, Phys. Rev. Lett. **79**, 4589 (1997).
[25] Y. Yang and H. Wu, J. Appl. Phys. **80**, 3699 (1996).
[26] L. D. Tsendin, Plasma Sources Sci. Technol. **4**, 200 (1995).
[27] Chin-Wook Chung, S. H. Seo, and H. Y. Chang (unpublished).
[28] I. B. Bernstein and T. Holstein, Phys. Rev. **94**, 1475 (1954).
[29] L. D. Tsendin, Zh. Eksp. Teor. Fiz. **66**, 1638 (1974) [Sov. Phys. JETP **39**, 805 (1974)].
[30] A. Schwabedissen, E. C. Benck, and J. R. Roberts, Phys. Rev. E **55**, 3450 (1997).
[31] E. V. Karoulina and Yu. A. Lebedev, J. Phys. D **21**, 411 (1988).
[32] V. A. Godyak, R. B. Piejak, and B. M. Alexandrovich, Plasma Sources Sci. Technol. **1**, 36 (1992), and references therein.
[33] P. Horowitz and W. Hill, *The Art of Electronics* (Cambridge University Press, Cambridge, 1989), p. 266.
[34] G. R. Branner, E. M. Friar, and G. Medicus, Rev. Sci. Instrum. **34**, 231 (1963).
[35] Yu. M. Aliev, I. D. Kaganovich, and H. Schlüter, Phys. Plasmas **4**, 2413 (1997).
[36] B. D. Fried and S. D. Conte, *The Plasma Dispersion Function* (Academic, New York, 1961).
[37] M. Surendra and D. B. Graves, Phys. Rev. Lett. **66**, 1469 (1991).
[38] C. G. Goedde, A. J. Lichtenberg, and M. A. Lieberman, J. Appl. Phys. **64**, 4375 (1988).
[39] G. Dilecce, M. Capitelli, and De Benedictis, J. Appl. Phys. **69**, 121 (1991).
[40] R. A. Stewart, P. Vitello, and D. B. Graves, J. Vac. Sci. Technol. B **12**, 478 (1994).